ACS APPLIED MATERIALS & INTERFACES

Research Article

www.acsami.org

Mechanically Robust Superhydrophobic Steel Surface with Anti-Icing, UV-Durability, and Corrosion Resistance Properties

Nan Wang,[†,‡,§] Dangsheng Xiong,*[,†,‡,§] Yaling Deng,[†] Yan Shi,[‡] and Kun Wang[§]

[†]School of Materials Science and Engineering, Nanjing University of Science and Technology, Nanjing 210094, Jiangsu, P. R. China
[‡]Jiangsu Key Laboratory of Advanced Micro/Nano Materials and Technologies, Nanjing 210094, Jiangsu, P. R. China
[§]Synergetic Research Center on Advanced Materials (SRCAM), Nanjing 210094, Jiangsu, P. R. China

Supporting Information

ABSTRACT: A superhydrophobic steel surface was prepared through a facile method: combining hydrogen peroxide and an acid (hydrochloric acid or nitric acid) to obtain hierarchical structures on steel, followed by a surface modification treatment. Empirical grid maps based on different volumes of H_2O_2/acid were presented, revealing a wettability gradient from "hydrophobic" to "rose effect" and finally to "lotus effect". Surface grafting has been demonstrated to be realized only on the oxidized area. As-prepared superhydrophobic surfaces exhibited excellent anti-icing properties according to the water-dripping test under overcooled conditions and the artificial "steam-freezing" (from 50 °C with 90% humidity to the −20 °C condition) test. In addition, the surfaces could withstand peeling with 3M adhesive tape at least 70 times with an applied pressure of 31.2 kPa, abrasion by 400 grid SiC sandpaper for 110 cm under 16 kPa, or water impacting for 3 h without losing superhydrophobicity, suggesting superior mechanical durability. Moreover, outstanding corrosion resistance and UV-durability were obtained on the prepared surface. This successful fabrication of a robust, anti-icing, UV-durable, and anticorrosion superhydrophobic surface could yield a prospective candidate for various practical applications.

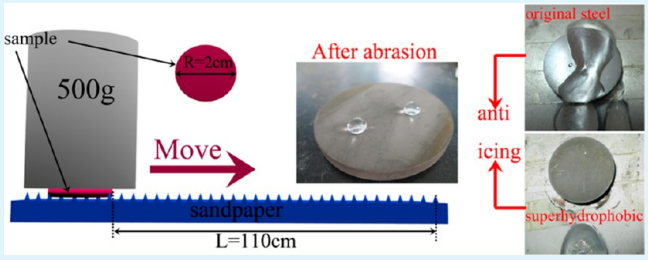

KEYWORDS: *superhydrophobic, mechanical durability, anti-icing, UV-durable, corrosion resistance, wettability gradient*

INTRODUCTION

Superhydrophobic surfaces have attracted tremendous scientific interest. Inspired by the lotus,[1−3] salvinia,[4,5] water-strider legs,[6,7] rose petals,[8,9] and gecko's feet,[10,11] a number of surfaces with special wetting behavior have been developed. These surfaces, which have static contact angle above 150°, promise a wide range of potential applications in self-cleaning,[12−14] anti-icing,[15,16] anticorrosion,[17,18] oil/water separation,[19−21] medical science,[22,23] drag reduction in fluid flow,[24,25] etc. It is widely accepted that low surface energies and high surface roughness values are required to fabricate a superhydrophobic surface. A lot of effort has been devoted to understanding the surface morphology of superhydrophobic materials and then to mimic their structure to improve the water repellency. Among these surfaces, the biomimetic structure of a lotus, which comprises of micro−nano hierarchical structure, is believed to provide outstanding superhydrophobicity and is accepted by most researchers.[3,26−29]

Methods to achieve superhydrophobicity can be classified into two categories:[30] (a) modifying a rough surface with low surface energies and (b) preparing a rough surface from a low surface energy material. Various methods have been developed to prepare a rough surface for large-scale applications, such as electrochemistry,[31] mechanical machining,[32] topography transfer,[33] and lamination;[34] chemical etching is the common way to create a rough surface morphology on metal. An acid or base solution is often chosen to corrode the metal surface and obtain hierarchical structures. Nakayama et al. prepared hierarchical structures on pure aluminum sheets through $CuCl_2$/HCl etching;[35] Yang et al. fabricated a superhydrophobic surface on pure aluminum plates by HCl corrosion and boiling-water treatment.[36] Preparing a superhydrophobic surface on steel through the combination of H_2O_2 and HCl/HNO_3 is relatively recent and is still scarcely reported.[37,38] To the best of our knowledge, only a few papers have reported a similar method to etch the substrate: Xiu et al. prepared a superhydrophobic surface on Si by the etching of HF and H_2O_2 method,[37] and Gupta et al. designed the surface structures on AZ31 alloy using the combination of H_2SO_4 and H_2O_2.[38] However, the mechanical durability of the aforementioned surfaces is not strong, which will be discussed in the following sections. The other key point in achieving a superhydrophobic surface is the low surface energy modification. Here, low surface energy silanes are chosen to modify the surface. During the self-assembly process, organosilanes are hydrolyzed by water to create the corresponding hydroxysilane [i.e., $RSi(OH)_3$]. The surface −OH groups work

Received: January 19, 2015
Accepted: March 6, 2015
Published: March 6, 2015

DOI: 10.1021/acsami.5b00558
ACS Appl. Mater. Interfaces 2015, 7, 6260−6272

as anchoring points for the formation of a covalent bond with the surface Si−OH. Thus, the sufficient density of surface −OH groups could help to improve the surface grafting efficiency and to form stable low surface energy monolayers. It is worth noting that oxidized films are formed after most metal-etching processes;[39−41] however, as compared with the surface morphologies, the extent to which the oxidized films influence the surface wetting and the modification efficiency of fluorosilanes has not been sufficiently investigated. In fact, the surface of oxides could form surface-bound hydroxyl (i.e., −OH) after being exposed to humid air or upon activation treatment.[42] Therefore, the surface of an oxidized metal is an excellent substrate for the grafting of low surface energy hydroxysilane.

One of the problems hindering the large-scale application of a superhydrophobic surface is the poor mechanical durability. Most of the currently prepared superhydrophobic surfaces, including the lotus leaves in nature, are incapable of resisting mechanical damage: the fragile micro−nano hierarchical structures are prone to be destroyed after a slight scratch, abrasion, impacting, and even finger touch,[43] to say nothing of peeling with adhesive tape or the abrasion by the sandpaper. Although some mechanically durable superhydrophobic surfaces have been reported, they actually rely on an intrinsic durable media, such as fabric,[44−46] polymer,[47,48] or metal meshes.[49,50] Achieving mechanically durable superhydrophobicity without introducing external media (i.e., on a flat metal surface) is still a great challenge. Besides, UV-durability and anticorrosion properties are equally crucial for practical outdoor use, which mainly depends on the surface chemical composition and surface structures. Notably, 1045 steel is one of the most important engineering materials and it has been used widely in construction and machinery. Therefore, it is of great significance to create a superhydrophobic steel surface with excellent mechanical durability and UV-durability, as well as anticorrosion ability.

Using the superhydrophobic surface to prevent or delay the freezing process is relatively recent and has been a hot topic for investigation considering the outstanding water repellency of superhydrophobic surfaces. The main reasons for the anti-icing properties of a superhydrophobic surface could be ascribed to the following: one is the removal of water before it freezes and the other one is the delay of crystallization caused by the lower freezing point or the barrier for heat transfer. Jiang et al. prepared anti-icing coatings with self-lubricating liquid;[51] Boinovich et al. fabricated icephobic coatings by etching steel with $FeCl_3$ solution[52] that exhibited good anti-icing properties in a natural environment. Though various superhydrophobic surfaces with anti-icing properties have been developed, their anti-icing performance under different conditions has not yet been adequately examined,[53] especially in low-temperature and high-humidity environments.

Herein, we report a superhydrophobic steel surface with excellent mechanical stability and anti-icing property fabricated through the combination of H_2O_2 and acid (HCl or HNO_3) and subsequent treatment with 1*H*,1*H*,2*H*,2*H*-perfluorodecyltriethoxysilane (i.e., FAS-17). A systematic study was carried out with two series: the hydrochloric acid series and the nitric acid series. An empirical grid map regarding the different wetting behaviors based on the H_2O_2/acid ratio was drawn that is instructive and could provide guidance for repeated experiments. Surface modification efficiency and the etching reaction mechanism were analyzed, with special consideration given to the oxidation area. The prepared superhydrophobic surfaces exhibited superior anti-icing in both the water-dripping test and the "steam-freezing" test under −20 °C artificial environments. More importantly, the prepared superhydrophobic surfaces also displayed excellent mechanical durability according to the tape-peeling, coarse-sandpaper-abrading, and water-impacting tests. Meanwhile, the UV-durability and anticorrosion properties of as-prepared surfaces were also examined.

EXPERIMENTAL SECTION

Materials. 1*H*,1*H*,2*H*,2*H*-Perfluorodecyltriethoxysilane (97%) (FAS-17), hexane (98%), and hydrogen peroxide (30 wt % in water) were purchased from Sigma-Aldrich. Hydrochloric acid (37 wt %) and nitric acid (98 wt %) were obtained from Shanghai Lingfeng Chemical Reagent Co., Ltd. 1045 steel (composition: C, 0.42−0.50; Si, 0.17−0.37; Mn, 0.5−0.80) was used as the metal substrates and was machined to dimensions of 20 mm in diameter, and the pretreatment of substrate is discussed in the Supporting Information (SI).

Fabrication of the Superhydrophobic Surface. First, a different amount of HCl or HNO_3 was added into 10 mL of deionized water, and then the cleaned substrate was immersed gently into the acid solution. After 30 s, a different amount of H_2O_2 was added quickly into the mixed solution. After reacting for 10 min, the substrate was rinsed with ethanol and desiccated in an oven. The volume of HCl or HNO_3 was varied from 0.5 to 3 mL (0.5 mL as an unit), while addition of H_2O_2 was varied from 0 to 3 mL (0.5 mL as an unit). Finally, the surface was soaked in 5 wt % FAS-17 in hexane at 40 °C for 2 h. The samples were then thoroughly cleaned with hexane and desiccated in a drying oven. After modified by FAS-17, samples prepared by the etching of HCl and H_2O_2 are labeled as A series, while those prepared by the etching of HNO_3 and H_2O_2 are denoted as B series; 42 different combinations of acid and H_2O_2 were performed for each series.

Anti-Icing Tests. Anti-icing tests were carried out in two ways: water dripping in an overcooled condition and a steam-freezing process.

The water-dripping test in cold conditions was performed in a self-made anti-icing chamber, which is presented schematically in Figure 1.

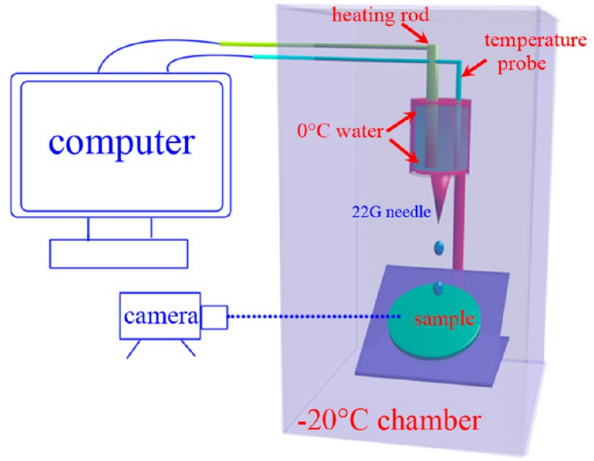

Figure 1. Schematic diagram of the setup for water dripping in overcooled conditions.

Deionized water used for the dripping process was placed in a syringe with a temperature monitor system and a heating rod. The sample was placed on a surface with sliding angle of 30°, and the distance between the surface of sample and the 22 gauge needle equipped on the syringe was 10 cm. First, the sample and water were placed in the chamber and the temperature was adjusted to −20 °C. During the cooling process, when temperature was under 0 °C, the water temperature was kept around 0 °C all the time by the heating rod so as to avoid the freezing of the water. Subsequently, the water-dripping process started when the temperature of the sample and water were stable. Here, the surface was treated with ∼50 μL droplets at a rate of three droplets per second, and

DOI: 10.1021/acsami.5b00558
ACS Appl. Mater. Interfaces 2015, 7, 6260−6272

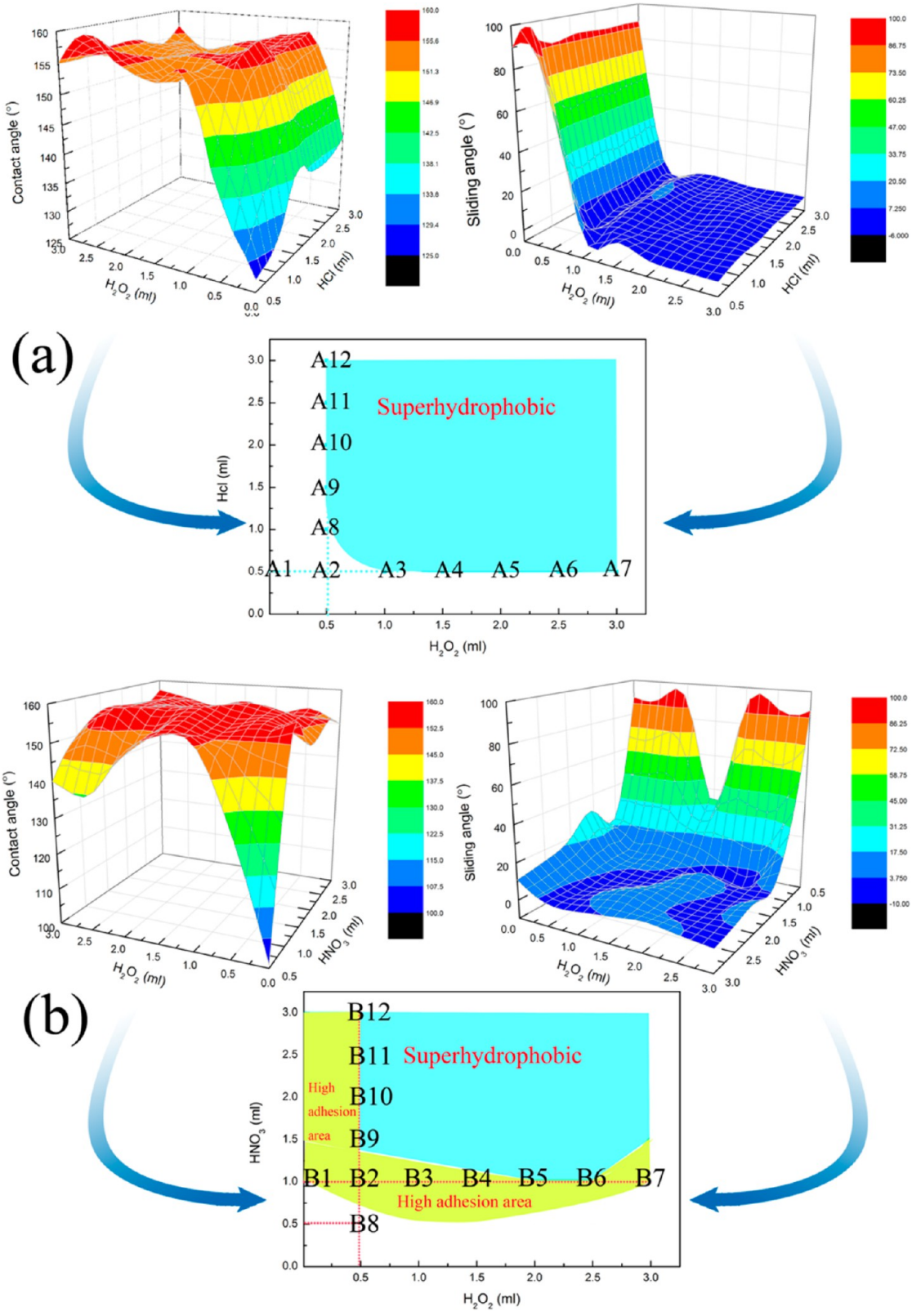

Figure 2. Surface wetting behaviors of (a) A and (b) B series.

the impact velocity was ~1.4 m/s. Finally, after 20 min (~3600 water droplets), the freezing area on the surfaces was recorded with a camera.

The steam-freezing process was carried out in a humidity chamber. First, the sample was exposed in the humidity chamber and then the temperature was adjusted to 50 °C with a wind of 90% relative humidity. Second, the humid wind was stopped and the temperature was adjusted to −20 °C. As the temperature decreased, water steam would condense into the liquid phase on the surface of all the samples and eventually turn into ice below the freezing point.

Mechanical Durability Tests. Tape-peeling, abrasion, and water-impacting tests were performed to assess the mechanical durability of as-prepared superhydrophobic surfaces.

DOI: 10.1021/acsami.5b00558
ACS Appl. Mater. Interfaces 2015, 7, 6260−6272

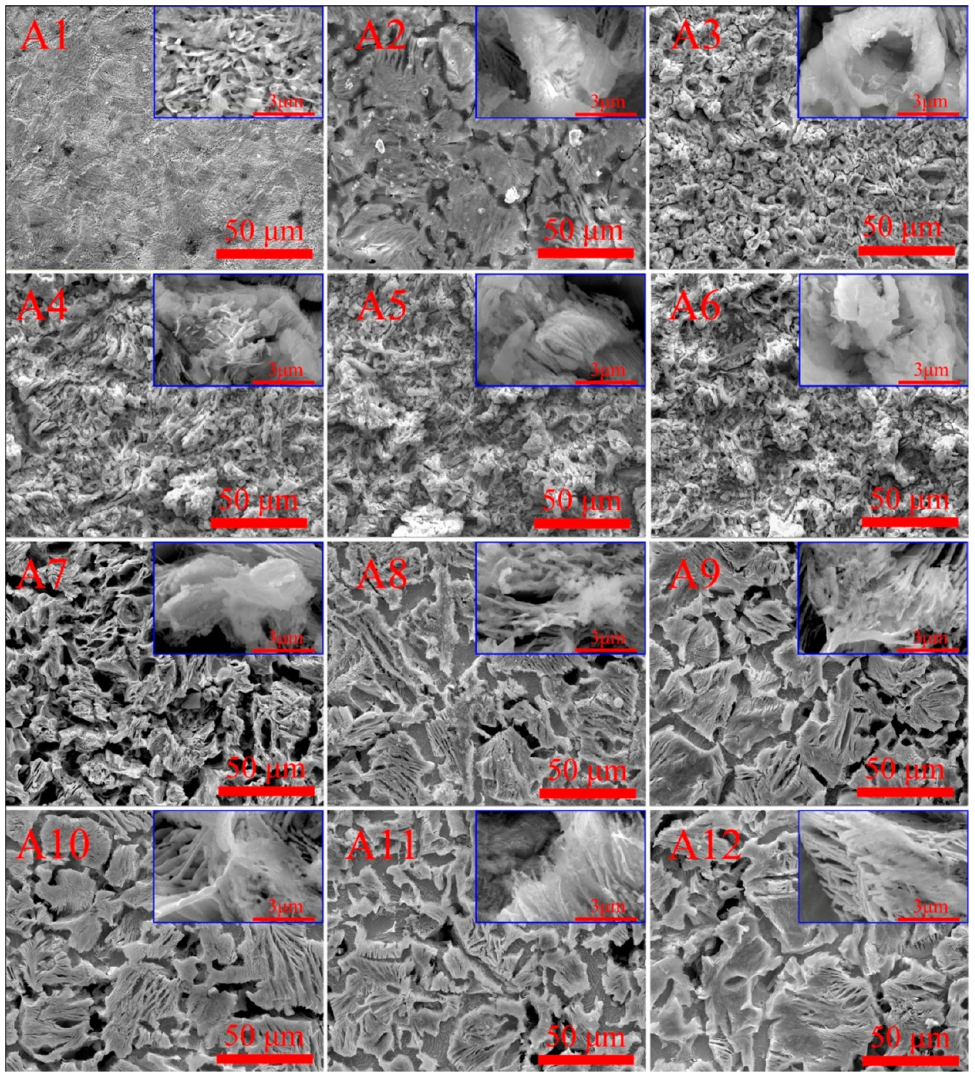

Figure 3. FE-SEM images of the A series.

Tape peeling was conducted with a standard method. Testing procedures were generally method B of ASTM D 3359-09$^{\varepsilon 2}$. The surface was pressed with adhesive tape and then the tape was peeled off. A thin eraser was attached under the loading so as to ensure that good contact was made between the sample and tape. Here, 31.2 kPa (1 kg loading on sample) pressure and Scotch-600 tape were employed to perform the test.

The second mechanical durability test was related to the abrasion/wear. The prepared surface was loaded with 500 g of force, facing 400 grid SiC sandpaper as an abrading surface, and moved forward in one direction at a rate of ∼6 cm/s. The gravity of the weight can be calculated as 16 kPa (including the weight of sample).

The water-impacting test was carried out using the reported method:[54] the prepared sample was treated with ∼100 μL droplets falling from 30 cm. The corresponding impacting velocity was ∼2.5 m/s at a rate of one drop per second. Sample was placed at a sliding angle of 45°.

UV-Durability Test. An UV chamber equipped with a 500 W ultraviolet high-pressure mercury lamp (Belsri/UV model, Beijing Institute of Electric Light Source) was used for irradiation, and static water contact angle and sliding angle of the samples were measured every 1 h. A film filter was used to restrict the passage of ultraviolet light within wavelengths of 350 ± 50 nm. Samples were placed in the UV chamber for up to 50 h at 50 °C.

Characterization. Water contact angles and sliding angles were determined with a 5-μL droplet of deionized water at ambient temperature on a contact angle measurement instrument (JC2000D2, Shanghai Zhongchen Digital Technology Apparatus Co., Ltd.) via a CCD camera. The surface morphology and surface element compositions were analyzed by a field-emission scanning microscope (FE-SEM, FEI Quanta 250F) equipped with an energy-dispersive spectroscope (EDS, Oxford). The distributions of detected elements were determined using the mapping mode. A true color confocal microscope system (Axio CSM 700) was used for morphology observation and surface roughness measurements. A digital camera (A3400IS, Canon) was used to record the anti-icing process and the mechanical durability tests. The anti-icing properties were investigated in a humidity chamber (RGDS-500, Surui Instruments Co., Ltd.).

The electrochemical corrosion test was carried out in a three-electrode cell at room temperature. Potentiodynamic polarization curves were measured in 3.5 wt % NaCl aqueous solution by a electrochemical workstation (VersaSTAT 3 system, Princeton) with a saturated calomel as reference electrode and platinum as the counter electrode, and sample was mounted using silicone with a surface area of 3.14 cm^2 (Ø 2 cm) exposed in the corrosive solution. The potentiodynamic polarization was recorded at the scanning rate of 1 mV/s from −200 to 200 mV versus the E_{ocp} (open circuit potential).

RESULTS AND DISCUSSION

Concerning the systematic study of the A and B series, 42 points (i.e., the number of experiments for each series) were carried with respect to the increasing concentration of H_2O_2 (from 0 to 3

DOI: 10.1021/acsami.5b00558
ACS Appl. Mater. Interfaces 2015, 7, 6260−6272

mL) and acid (from 0.5 to 3 mL) as described in the Experimental Section. The static contact angle and dynamic contact angle images of series A (i.e., HCl + H_2O_2 series) and B (i.e., HNO_3 + H_2O_2 series) are presented in Figure S1 and S2 in the SI, respectively. As shown, different wetting behaviors could be observed with respect to the varying volume of acid or H_2O_2. To further study the effect of acid and H_2O_2 on the wetting behaviors, contact angle and sliding angle as a function of acid and H_2O_2 volume are presented in 3D diagrams (volume of H_2O_2 as *X* axis, acid as *Y* axis, contact angle or sliding angle as *Z* axis) for A and B series. Moreover, empirical grid maps were drawn on the basis of the 3D diagrams, illustrating different wetting behavior regions as shown in Figure 2.

As can be seen, three different hydrophobic regions could be obtained: hydrophobic, high static contact angle with high droplet adhesion, and low adhesion regions. With the increase of H_2O_2, the static contact angle remained above 150°, while the wetting behavior varied from remarkable high adhesion to extremely low adhesion, which could also be regarded as the change from the "rose effect" to the "lotus effect", showing a gradient change. It is worthwhile to note that only in the B series (i.e., HNO_3 + H_2O_2 series) could the high water adhesion area be obtained. For the A series (i.e., HCl + H_2O_2 series), the surface wettability exhibited a striking contrast: only the "hydrophobic" area and the "superhydrophobic" area could be obtained; no transition area (i.e., high adhesion area) could be observed compared with the B series.

Here, samples that reflected the variation of wetting behavior were chosen and denoted as A1−A12 and B1−B12, as shown in Figure 2. This grid map is instructive and can provide empirical guidance for other researchers.

Surface Etching Process. FE-SEM images with different magnifications of the A series are displayed in Figure 3. For the samples A1−A7 (i.e., HCl was kept unchanged and H_2O_2 increased, as shown in Figure 2a), the surface morphologies exhibited a significant difference: on the low-magnification level, the surface of A1 was relatively smooth, and the surfaces showed an increasing damage and corrosion phenomena with the increase of H_2O_2; on the high-magnification level, there can be seen different kinds of microscale asperities. This is because defects (e.g., dislocation) exist in common crystalline metals owning relatively high energy, which makes it easier to be attacked by chemical etchants and dissolved first. This selective corrosion behavior would render the surface roughness and the asperities.[40] With the increase of H_2O_2, the crack would spread out and more severe corrosion effects could be observed (A1−A7 in Figure 3). Similar conclusion could also be obtained in B series (Figure S3, SI).

As for the samples A2 and A8−A12 (i.e., H_2O_2 was kept unchanged and HCl increased, as shown in Figure 2a), it seems that there was no significant difference between the surface morphologies on both the high and low magnification images. In contrast, the surface morphologies show noticeable differences in B2 and B8−B12 samples in Figure S3 (SI) (i.e., H_2O_2 was kept unchanged and HNO_3 increased). The different surface corrosion behavior between A and B series could be ascribed to following: the nitric acid itself is a powerful oxidizing reagent; thus, more severe etching could be provided to the surface than the hydrochloric acid did.

Figure 4a shows the schematic view of the etching process. As known, H_2O_2 exhibits an extremely strong oxidizing property in acid solution, which means that Fe could be oxidized into Fe_2O_3 in the reacting solution for both A and B series. This could promote the surface-etching process and the reacting rate because the reaction between the Fe_2O_3 and acid is merely a dissolution reaction, while the reaction between the Fe and acid (HCl or HNO_3) is an oxidation reaction. The reacting process can be described by the following equations:

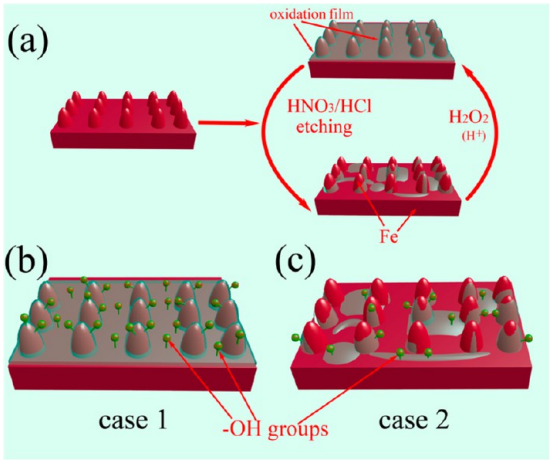

Figure 4. (a) Schematic view of the reacting process. Surface hydroxyl on the oxidation surface (b) before and (c) after the chemical etching.

$$2Fe + 3H_2O_2 \xrightarrow{H^+} Fe_2O_3 + 3H_2O \quad (1)$$

$$Fe_2O_3 + 6H^+ \rightarrow 2Fe^{3+} + 3H_2O \quad (2)$$

Overall, the addition of H_2O_2 could help to accelerate the reacting process and promote the corrosion behavior, because the oxidizing nature of hydrogen peroxide has been promoted in acidic condition,[55] which would influence the diversification of the wetting behavior and the surface grafting efficiency, as described in the following discussion.

Surface Grafting Analysis. EDS spectra and wetting behaviors of A and B series at 2000× magnification are presented in Figures S4 and S5 in the SI, respectively. The presence of fluorine element has been confirmed on the samples in the superhydrophobicity area (Figure 2), indicating the successful grafting of the FAS-17 molecules. The distribution of F, O, and Fe of A2−A7 are displayed in Figure 5. As can be seen from the EDS mapping images, the Fe element, from the steel substrate, exhibited a uniform distribution for all samples. It is found that the O on all surfaces exhibited a heterogeneous distribution, which is in coordination with the bright area shown in the FE-SEM images. One could observe that the distribution of F and O showed a surprising consistency and that F could barely be detected in the regions without O element. Meanwhile, according to EDS spectra, the amount of O on the surface was much more than that existing in the FAS-17 molecules (calculations will be presented in the following discussion section), indicating that the similar distribution of F and O was not due to the introduction of ethoxy by the silane itself. Accordingly, it is reasonable to conclude that the surface grafting of FAS-17 only happened on the local area where there is large amount of O element; in another words, surface modification/grafting could only be carried out on oxidized region. This can be ascribed to the −OH groups that existed on the oxidized surface, which is believed to be the prerequisite for surface grafting of silane. In fact, for most of the superhydrophobic surfaces fabricated on the metal substrates through various methods, the oxidized surface always appears.[56−58] Comparing the surface

DOI: 10.1021/acsami.5b00558
ACS Appl. Mater. Interfaces 2015, 7, 6260−6272

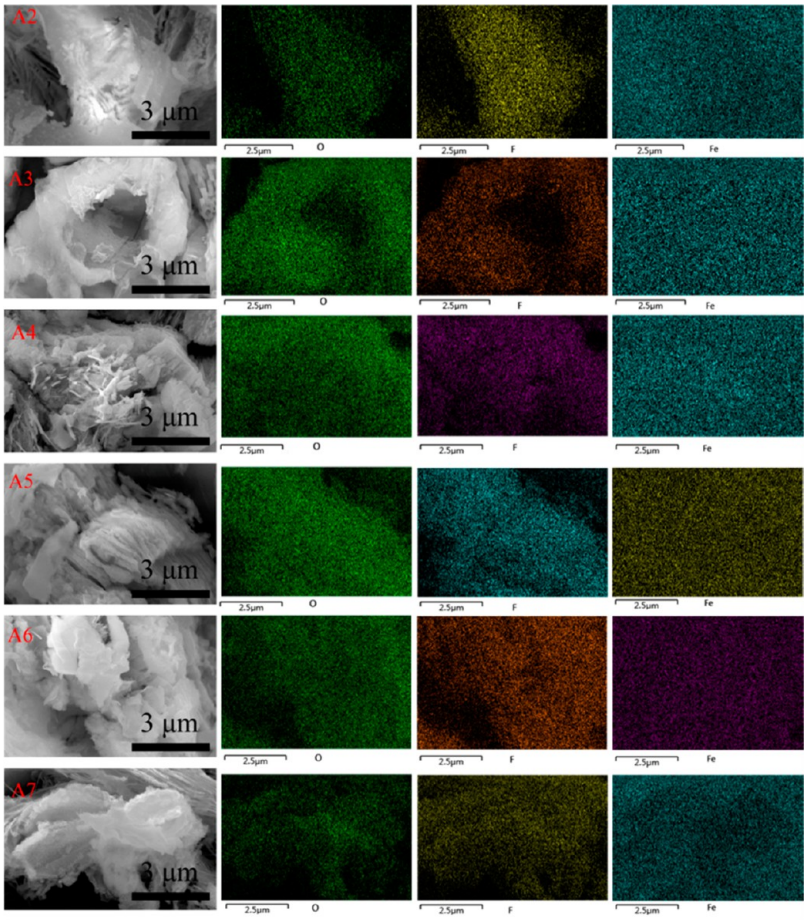

Figure 5. EDS mapping images of F, O, and Fe elements of A2−A7.

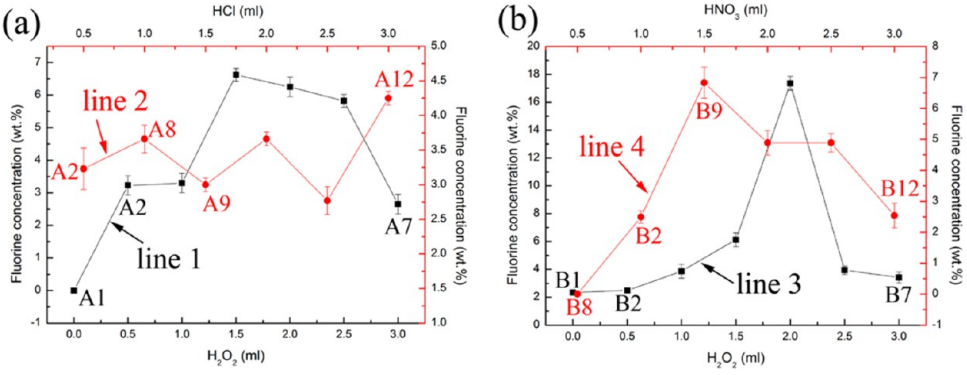

Figure 6. Content of F element of (a) A and (b) B series.

structures, the surface modification has not attracted sufficient attention, especially the oxidized layer. The surface of oxides possesses surface-bound hydroxy groups after being exposed to humid air, which could work as the anchoring points, because a covalent linkage could be formed between the hydrolyzed silane and the surface −OH groups.[42] Therefore, it is only on the oxidized area that the FAS-17 can be grafted to the steel surface, which in turn explains the analogous distribution of O and F. Similar conclusions were obtained for the B series. So, using the combination of H_2O_2 and HCl (or HNO_3) to etch 1045 steel, one could achieve both the micro−nano hierarchical structures and the surface hydroxylation at the same time.

The content of F element of A and B series is shown in Figure 6. As can be seen from the lines 1 (i.e., A1−A7) and 3 (i.e., B1−B7), the content of F element on the surfaces increased along with the addition of H_2O_2 until a critical point was reached, and it then went down to a certain value, showing a synchronous step. Especially for A1, the F could barely be detected without the H_2O_2 during the fabrication process. This is because the etching−oxidation process was in a dynamic cycle: at the beginning of the addition of H_2O_2, the area of the oxidation surface increased, which in turn could promote the modification and the grafting of FAS-17 molecules due to the large amount of −OH formed on the surface, as described in Figure 4b; at the same time, the etching rate (i.e., the dissolution of the oxidation

DOI: 10.1021/acsami.5b00558
ACS Appl. Mater. Interfaces 2015, 7, 6260−6272

layer) also accelerated and the surface corrosion was more severe with increasing H_2O_2 [see FE-SEM images in Figures 3 and S3 (SI)], which means the dissolution amount of oxidation film was increasing and more Fe^{3+} could be introduced into the solution. When the amount of H_2O_2 reached a certain point (i.e., critical point), the Fe^{3+} also reached a critical concentration, and then the H_2O_2 decomposed into H_2O and O_2 under the catalysis of Fe^{3+}, as described in the following equation:

$$2H_2O_2 \xrightarrow{Fe^{3+}} 2H_2O + O_2\uparrow \quad (3)$$

At this moment, large amounts of air bubbles could be observed in the reacting solution, and some of the solution overflowed (Figure S6, SI), indicating the decomposition reaction of H_2O_2. Meanwhile, the surface etching was still occurring, and there was not enough H_2O_2 left for the newly born surface (i.e., surface formed after etching) to form a wide range of oxides on the surface, thereby resulting in the decline of the oxidation area and the surface grafting efficiency (i.e., the content of F element) as described in Figure 4c. Thus, the concentration of Fe^{3+} and H_2O_2 is very crucial for the surface grafting. To benefit the surface grafting efficiency, the addition of H_2O_2 should be limited in a certain range.

When the H_2O_2 volume was kept constant, different surface grafting behavior could be observed: for line 4 (i.e., B series), the content of F first increased and then declined to a certain point, indicating the decline of surface grafting efficiency; as for the line 2 (i.e., A series), the content of F stayed relatively stable. This is because the HNO_3 itself is a powerful oxidant and could provide a more severe etching effect and larger oxidized area for the metal, as discussed above, which means that more oxidized area could be dissolved by the HNO_3 than by the HCl, promising a higher concentration of Fe^{3+} and subsequently more decomposition of H_2O_2. On the other hand, along with the increase of HNO_3, after the etching process, there was not enough H_2O_2 left to meet the need for the oxidation of metal surface, thus resulting in the decrease of oxidation surface and the declined modification efficiency of line 4. In a word, the concentration of acid in the reacting solution is also important for the surface grafting efficiency.

To sum up, the concentration of H_2O_2 and acid could directly influence the formation of an oxidized film on the steel, which has profound influence for the modification efficiency and the wetting behavior.

Wetting Behavior Analysis. In order to further study the relationship between surface morphology and wetting behavior, a true color confocal microscope was introduced to characterize the surface of prepared sample. The 3D view of A6 is shown in Figure 7a, and other images of A and B series are presented in Figures S7 and S8 in the SI, respectively. One could observe that microscale asperities could be obtained on the surfaces within the "superhydrophobic" area shown in Figure 2. Meanwhile, nanoscale asperities could also be observed on these microscale structures, as shown in Figure 7b. The nanoscale asperities are almost the same on all samples of the A and B series. It is clearly evident that the samples in this area comprise micro−nano hierarchical structures on the surfaces. Besides, as shown by the EDS spectrum (Figure 7c), an obvious F peak could be observed, indicating the FAS-17 was successfully grafted on the surface and that the surface was endowed with low surface energy property. Accordingly, the micro−nano hierarchical structures, combined with the low surface energy compositions, are consistent with those of lotus leaves.[1] On the other hand, the content of O and F

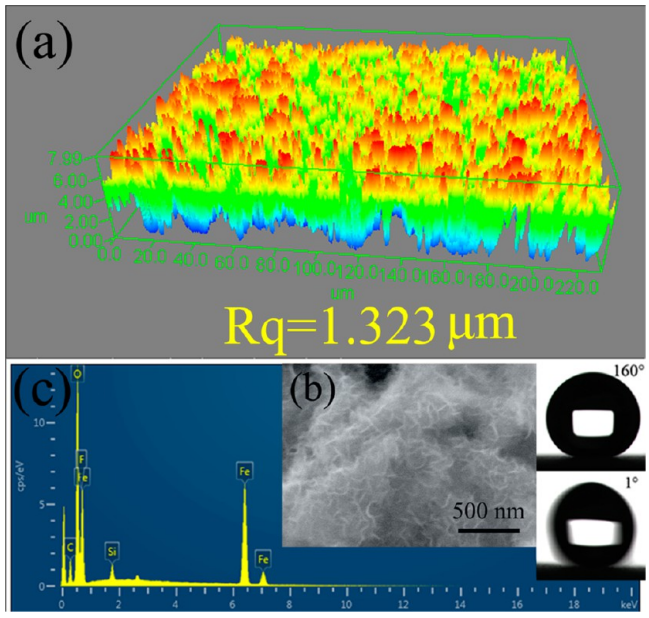

Figure 7. (a) True color confocal microscope images, (b) FE-SEM images, and (c) EDS spectrum and wetting behavior of A6.

element is about 23 and 6.3 wt % according to Figure 7c, and the corresponding content of O introduced by the FAS-17 is about 0.93 wt %, which is far smaller than the content of O on the surface, demonstrating that the large area of O distribution shown in EDS mapping images (Figure 5) was not due to the surface grafting of FAS-17.

Nanoscale structures can be seen from FE-SEM images (Figure 7b), the size of asperities or the distance of adjacent asperities is less than 100 nm. According to the theory of Chandler,[59] for a water droplet at room temperature and atmospheric pressure, there is a critical distance, $D_c \approx 100$ nm, which is a prerequisite for air trapping between two hydrophobic plates. When water droplets sit on the surface, these nanoscale asperities will create excluded volume regions where the density of water molecules vanishes,[17] thereby resulting in the sufficient air pockets trapped in the surface. Figure 8a,b display the Rq curves of all samples. For A series, A1 and A2 samples exhibited low contact angle and high sliding angle; this is because the surface roughness and the content of F on the surface are much lower than for other samples in the A series, which could lead to the loss of hydrophobicity. As for the samples in B series, the transition from rose effect to lotus effect could be observed. According to Figures 6b (i.e., content of F element) and 8b (i.e., surface roughness), the surface samples in the lotus effect area contain higher surface roughness and a larger amount of F element compared to those in the rose effect area, thereby promising the better water repellency and lower sliding angle. On the other hand, a noticeable difference could be obtained between lines b and d (i.e., H_2O_2 was kept unchanged and acid was increased, as shown in Figure 2): the Rq values of line d exhibit a proportional relationship with the additional volume of acid, while the line b fluctuates in a certain range. This also manifested that the HNO_3 could provide more severe etching behavior for the steel surface. In order to understand the relationship between the static contact angle and the micrometer roughness, the Rsk^m (skewness of roughness file) of A series, indicating the degree of symmetry of surface heights about the mean plane, was revealed to be related to the static contact angle.

DOI: 10.1021/acsami.5b00558
ACS Appl. Mater. Interfaces 2015, 7, 6260−6272

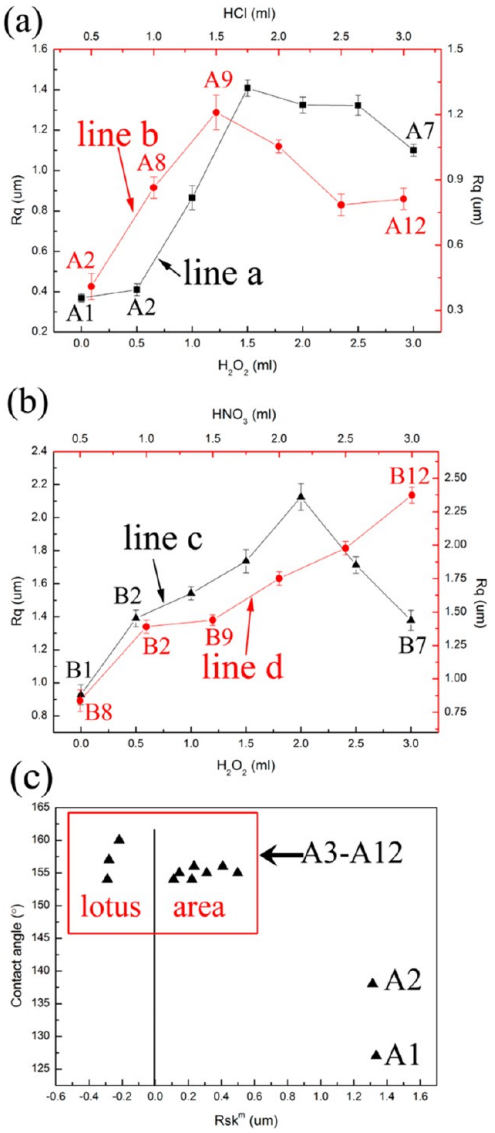

Figure 8. Rq curves of (a) A and (b) B series. (c) Static contact angle against the skewness of the roughness profile (Rsk^m) of A series.

The Rsk^m and contact angle values are displayed in Table S1 in the SI. As suggested by Boscher,[60] the superhydrophobicity could be obtained when the absolute values of Rsk^m are close to 0. As can be seen from Figure 8c, the Rsk^m of samples within the lotus effect area (Figure 2a) possess lower absolute values comparing to those (i.e., A1 = 1.335, A2 = 1.313) outside the area, which has afforded an impressive demonstration of Boscher's research.

Overall, for samples with Rsk^m absolute values close to 0, higher surface roughness and higher content of F element are generally consistent with the "superhydrophobic" area, as shown in Figure 2.

Anti-Icing Studies. Anti-icing properties are mainly related to the following three aspects: the removal of water/condensed water before it freezes, the delay in the crystallization of condensed water, and the constrained expansion of ice film. A6 was chosen to test the anti-icing properties.

The water-dripping test was carried out at −20 °C, and the water droplets were kept at 0 °C to mimic the natural environment. Figure 9 displays the comparative results after the test: the untreated surface was covered with ice, while a small

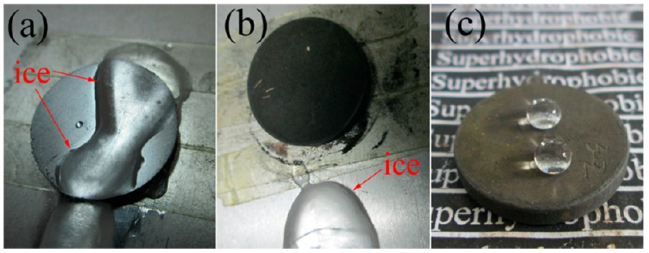

Figure 9. Comparison of the icing film on (a) original steel and (b) A6 surface. (c) Water droplets on A6 after the dripping test under overcooled condition. The surface still exhibited lotuslike water repellency.

frozen spot could barely be observed on the superhydrophobic surface. This can be attributed to the different water adhesion: when a droplet fell onto the untreated steel, it remained on the surface due to the hydrophilic nature, followed by freezing; in contrast, the drop rolled off easily on superhydrophobic surface, which makes it very hard to freeze within such short time. Samples after the water-dripping test still retained their extreme water repellency property (Figure 9c). The wetting behavior after dripping in overcooled conditions is displayed in Figure S9 in theSI: the static contact angle stayed unchanged and the sliding angle slightly increased to 2°.

In order to thoroughly study the anti-icing properties of prepared superhydrophobic surfaces, a steam-freezing test was performed to mimic the extremely condensing weather conditions in the natural environment. This test was mainly designed to access the ability of as-prepared samples to delay freezing/crystallization. During this process (i.e., from 50 °C with 90% humidity to the −20 °C condition), the water experienced three phases: gas, liquid, and solid. At the beginning time, with the increase of temperature and the air humidity, the chamber was filled with water steam (90% humidity). Then the temperature was adjusted to −20 °C, and the steam would condense into water and finally freeze below the solidification temperature. Figure 10a shows the comparable results of the steam-freezing test of the original steel and the superhydrophobic surface. As can be seen, a large ice film could be observed on the original steel, whereas an ice film, or even very small freezing spots, could hardly be found on the superhydrophobic surface.

The delayed freezing process could be ascribed to the lower freezing point of water on the superhydrophobic surface, which could be explained by Kelvin's law and the Clapeyron relationship.[61] The surface of prepared superhydrophobic surfaces is comprised of micro−nano hierarchical structures, which would lead to the formation of capillaries. The formula is shown below

$$P_r = P \exp\left(\frac{2\gamma V_m}{RTr}\right) \quad (4)$$

where P_r and P are the vapor pressure and saturated vapor pressure at a certain temperature, V_m is the molar volume of the phase, γ is the surface energy, R is the gas constant, T is the temperature, and r is the radius of the droplet or crystal. For an intrinsically hydrophobic surface, the interface is convex and r is positive. It is clear that the P_r is inversely proportional to r on a hydrophobic surface. For condensed water on a superhydrophobic surface, the diameter could be very small, promising a very large P_r value. As is known, such small droplets with high vapor pressure are not easy to contain; thus, the amount of water

DOI: 10.1021/acsami.5b00558
ACS Appl. Mater. Interfaces 2015, 7, 6260−6272

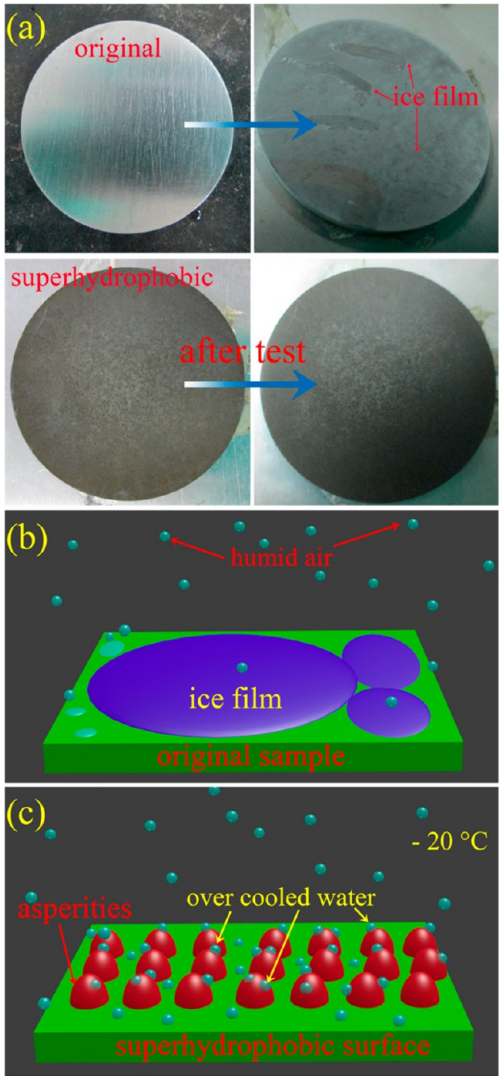

Figure 10. (a) Comparison of frost films on A6 after the steam-freezing (from 50 °C with 90% humidity to the −20 °C condition) test. Schematic view of the condensed small droplets on (b) original steel and (c) A6 surface.

condensed on the superhydrophobic surface was not much compared to that on the hydrophilic steel surface (Figure 10b).

On the other hand, for the solidification/freezing process, the Clapeyron formula could be transformed as follows

$$\frac{dT}{T} = \frac{T\Delta_s T_m}{\Delta_s H_m} dP \quad (5)$$

where T is the temperature, P is the vapor pressure, and $\Delta_s V_m$ and $\Delta_s H_m$ are the volume difference and enthalpy change during the solidification process, respectively. After integration of eqs 4 and 5, we get the following formula:

$$\ln \frac{T_2}{T_1} = \frac{\Delta_s V_m}{\Delta_s H_m}(P_2 - P_1) \quad (6)$$

During the freezing process, $\Delta_s V_m > 0$ and $\Delta_s H_m < 0$; therefore, T is inversely proportional to P. In another words, for condensed water on a superhydrophobic surface, the smaller the r is, the lower the freezing temperature would be. The schematic view of condensed water on a superhydrophobic surface is presented in Figure 10c. Compared with the bare substrate, condensed water on the superhydrophobic surface tends to be supercooled, and the freezing temperature of water decreased largely (below −20 °C). Therefore, when put into a cold environment along with the bare substrate, the very small droplets on the superhydrophobic surface could not freeze, thus retarding the icing.

In some area, the condensed water might have larger r due to the heterogeneous surface morphologies or insufficient low energy surface modification, which would lead to the higher freezing point for water (i.e., above −20 °C) according to above discussion and thereby lead to the appearance of small icing spots. In this case, the droplets would be isolated from each other due to the high static contact angle caused by the hydrophobic nature of the surface, which could constrain the formation of a broad water film and thus constrain the icing area after the solidification. So, for the larger condensed droplets, which have freezing temperature higher than −20 °C and are spherical in shape, this could help constrain the expansion of the icing film. If the droplets are large enough, they would roll off the surface due to gravity before freezing.

Mechanical Durability. One of the greatest problems hindering the large-scale use of superhydrophobic surfaces is their poor mechanical stability. Even a slight scratch or abrasive force could destroy the surface structure and thereby disable the superhydrophobicity. In an effort to assess the mechanical durability of prepared superhydrophobic surfaces, A6 sample was tested through tape-peeling, coarse-sandpaper-abrading, and water-impacting tests.

The tape-peeling test shows that the surface could resist tape peeling at least 70 times by Scotch-600 adhesive tape (for details, see Video S1, SI) without losing its superhydrophobicity. Figure 11 presents the contact angle and sliding angle as a function of

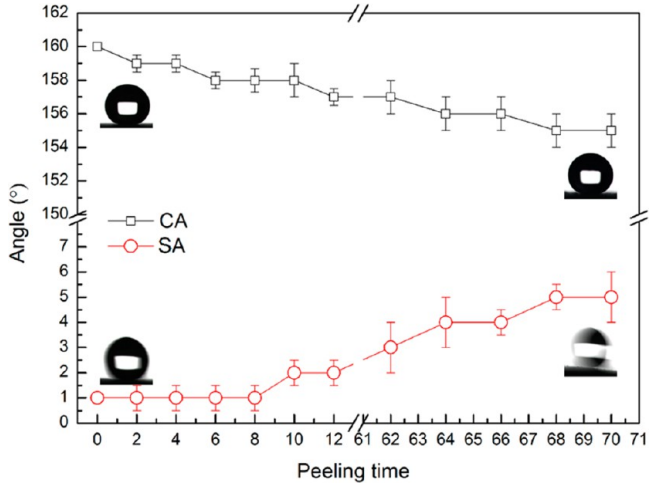

Figure 11. Contact angle and sliding angle as a function of peeling times for A6.

the number times the tape was peeled for the prepared superhydrophobic surface. As can be seen, after peeling with tape 70 times, the water repellency exhibited a slight decline, but it was still within the lotus effect category. We have provided harsher test conditions for the peeling test regarding the loading pressure as compared to other reported superhydrophobic surfaces.[62−65] The pressure we used to press the tape to the sample was 31.2 kPa (1 kg loading), which is much larger than the "finger press" described in the standard ASTM D 3359-09$^{\varepsilon 2}$ or 10 kPa applied on the superhydrophobic surface made from porous silica capsules.[62] Meanwhile, the tape we have chosen

DOI: 10.1021/acsami.5b00558
ACS Appl. Mater. Interfaces 2015, 7, 6260−6272

could provide more adhesive force as compared to the Scotch 810 tape used on the copper.[63] Besides, we repeated the peelings up to 70 times, which is much more than other reported work,[65] not to mention conducting the tape peeling under such high pressure. In a word, according to the tape-peeling test, the prepared steel surface showed excellent mechanical durability.

A schematic view of the abrasion test is shown in Figure 12a. A 500 g loading was applied to the prepared sample, and 400 grid

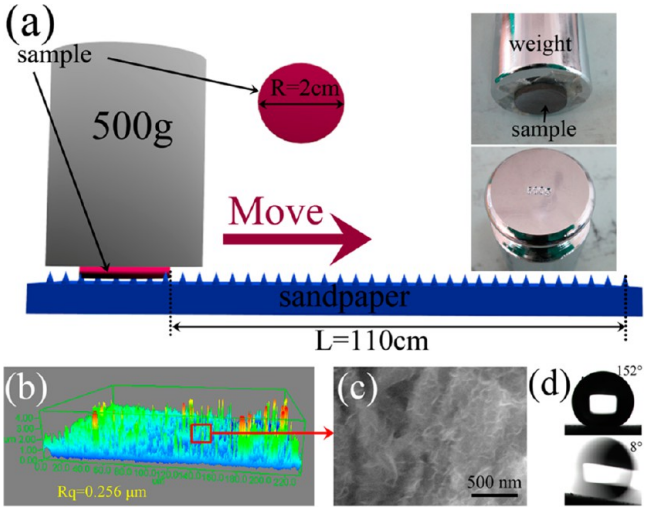

Figure 12. (a) Illustration of the abrasion test for A6 surface at 500 g loading on sandpaper (400 grid SiC). (b) 3D view of microscale structures, (c) nanoscale asperities, and (d) wetting behavior of A6 after the abrasion test.

SiC sandpaper was used as the abrading surface. The surface was dragged in one direction for 110 cm under 16 kPa pressure (for details, see Video S2, SI). After the abrasion, the water repellency showed almost no change and the water drops maintained a spherical shape, as shown in Figure S10 in the SI. The wetting behaviors after abrasion are shown in Figure 12d: the static contact angle decreased from 160° to 152°, and the sliding angle increased to 8°. On the basis of the above experimental results, the as-prepared surface could still retain its superhydrophobicity after the abrasion. In fact, the results displayed above show better mechanical durability than other reported superhydrophobic surfaces formed on metal/Si surface in recent years:[37,55,66−70] the superhydrophobicity on the Si surface disappeared after 25 cm of abrasion on a wipe under 3.45 kPa pressure;[37] the superhydrophobic surface formed on copper could not endure abrasion for 1.0 m at an applied pressure of 6.0 kPa on 800 grid sandpaper[66] or was damaged after being scratched for 40 cm at 0.69 kPa on 5000 grid sandpaper;[70] the contact angle decreased largely (170° vs 153°) after abrasion under 5 kPa by cotton fabric ($40^s \times 40^s$) for only 25 cm;[55] a similar surface formed on aluminum alloys could not withstand 90 cm of abrasion at 10 kPa pressure on 2000 grid sandpaper[67] or 15 cm of abrasion at 0.98 kPa pressure on 500 grid sandpaper;[68] the sliding angle largely increased (1.2° ± 0.9° vs 52.7° ± 1.4°) on magnesium alloy after 70 cm of abrasion on 800 grid sandpaper under the pressure of 1.2 kPa.[69] Briefly, compared to previous literature results, the as-prepared superhydrophobic surface showed excellent stability against abrasion.

Figure 12b displays the surface morphology obtained on the true color confocal microscope system after abrasion for 110 cm at 16 kPa on 400 grid sandpaper. Compared with the surface before abrasion in Figure 7a, the microstructures were partially damaged by the coarse sandpaper, and the surface root-mean-square roughness decreased from 1.323 to 0.256 μm; the height of the remaining microstructure decreased greatly comparing to that before abrasion. This ruined surface structure may contribute to the slight decline of the superhydrophobicity. Nevertheless, the surface still exhibited an extremely hydrophobic property. This can be rationalized in this way: after abrasion, microscale structures still existed on the damaged surface, which exhibited smaller size compared with ones before abrasion (Figure 7a); on the other hand, the FE-SEM image after the abrasion test shown in Figure 12c suggests the existence of nanoscale structures. This new hierarchical structure, though not as large as it was before abrasion, is the reason that the surface still exhibited superhydrophobicity.

The water-impacting test was conducted under the reported procedure.[54] The contact angle and sliding angle as a function of water-impacting time for the prepared superhydrophobic surface are presented in Figure 13a. As can be seen, the surface still showed a static contact angle above 153° and a sliding angle below 7° after 3 h (~10 800 droplets) of impacting, which further proved the outstanding mechanical stability of as-prepared superhydrophobic surface.

UV-Durability and Anticorrosion. In order to assess the UV-durability of the as-prepared superhydrophobic surface, the samples were exposed to UV light for 50 h at 50 °C, and the wetting behaviors were measured every 1 h. The static contact angle and sliding angle as a function of UV-irradiation time are presented in Figure 13b. As shown, after irradiation for 50 h, the

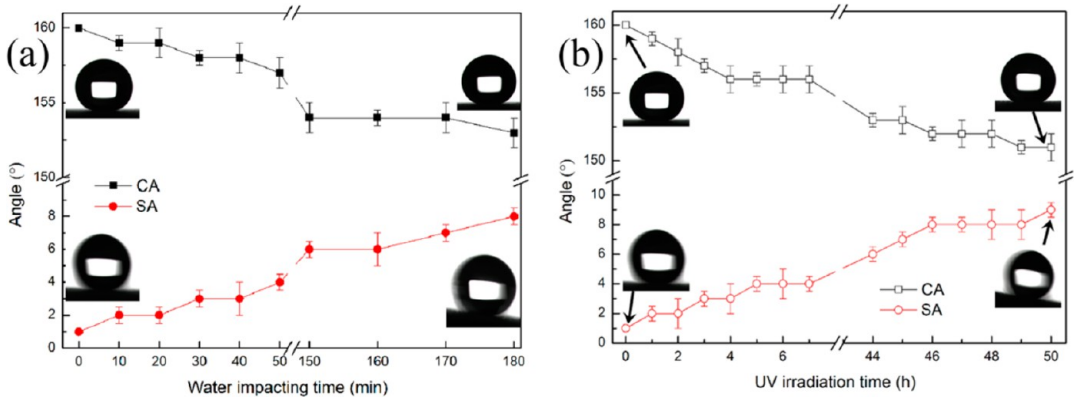

Figure 13. Contact angle and sliding angle as a function of (a) water-impacting time and (b) UV-irradiation time for A6.

DOI: 10.1021/acsami.5b00558
ACS Appl. Mater. Interfaces 2015, 7, 6260−6272

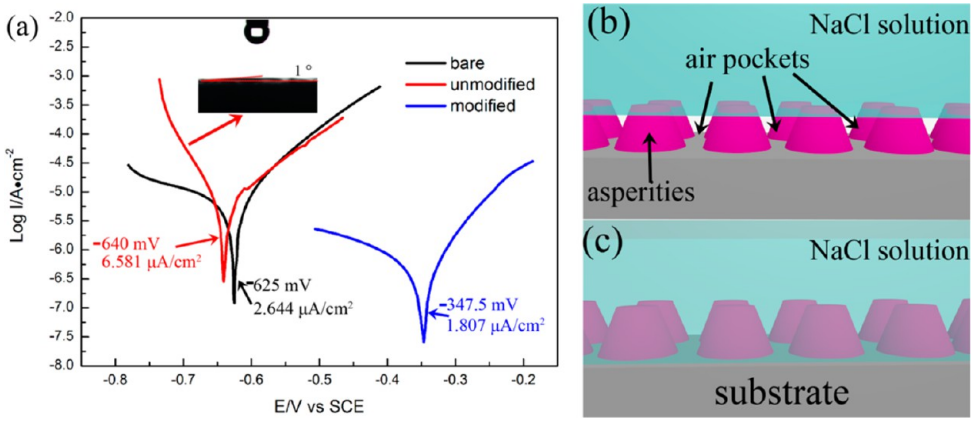

Figure 14. (a) Tafel plots of different treated samples and wetting behavior of unmodified A6 surface. Schematic views of corrosive liquid on (b) modified and (c) unmodified A6 surfaces.

surface still exhibited a contact angle of 151° and a sliding angle of 9°, suggesting a superior UV-durability. This can be ascribed to the long chain of FAS-17 on the surface, which can provide a large number of C−F bonds (i.e., $-(CF_2)_7-CF_3$ chain). This C−F bond, with a bond energy of 485 kJ/mol, cannot be broken by the UV light[71] (314−419 kJ/mol) as compared to the long alkane chain of HDTMS.[72] Therefore, to obtain the UV-durable superhydrophobic surface, modifying the surface with long chain of C−F is necessary.

In order to thoroughly study the stability of as-prepared superhydrophobic surfaces, we further investigated the corrosion resistance through the electrochemical corrosion test. Potentiodynamic polarization curves of the bare substrate, surface without modification and the superhydrophobic surface (A6 sample) were measured in 3.5 wt % NaCl aqueous solution, as shown in Figure 14a. The surface without modification and the superhydrophobic surface shared the same surface morphology. Parameters such as corrosion current (I_{corr}) and corrosion potentials (E_{corr}) can be derived from Figure 14a using the Tafel extrapolation. It can be easily found that the corrosion resistance ability was dramatically improved on the superhydrophobic surface due to the higher E_{corr} (−347.5 mV) and lower I_{corr} (1.807 $\mu A/cm^{-2}$) as compared to those of bare substrate (E_{corr} = −625 mV, I_{corr} = 2.644 $\mu A/cm^{-2}$), suggesting a good corrosion protection for the steel substrate. The presented anticorrosion property could be ascribed to the air pockets trapped in the surface micro−nano hierarchical structures.[73] The mechanism of the anticorrosion is shown in Figure 14b. When superhydrophobic surfaces are immersed in 3.5 wt % NaCl solution, due to the surface tension of water and the intrinsic hydrophobicity of the substrate, it is hard to penetrate into the micro−nano hierarchical structures, and the corrosive solution is isolated from most of the surface, thus achieving an "air protection shield" and better anticorrosion ability.

On the other hand, since the superhydrophobic surfaces have been oxidized, whether the good anticorrosion behavior observed is due to the barrier effect provided by the oxide layer or the superhydrophobic behavior is not clear. In order to address this concern, the corrosion behavior of the oxidized surface (i.e., surface containing hierarchical structures) without modification by FAS-17 was also evaluated by Tafel plot, as shown in Figure 14a. The contact angle of unmodified surface is about 1°. The schematic view of water on this kind of surface is shown in Figure 14c. The corrosive liquid could easily penetrate into the surface microstructures, because the surface is intrinsically superhydrophilic and full of −OH groups. Comparing with bare substrate, lower E_{corr} (i.e., −640 mV) and higher I_{corr} (i.e., 6.581 $\mu A/cm^{-2}$) could be found on the surface without modification. Clearly, this surface exhibited worse corrosion resistance than the bare substrate did, which means that the anticorrosion behavior shown by the FAS-17-modified surface is not due to the oxide layer. Therefore, the anticorrosion property of the superhydrophobic surface is merely due to the air protection shield and not the oxide layer barrier, as mentioned in reported work.[74,75] It is not clear whether the oxide layer could provide a barrier in corrosive liquid when applied to different metal substrates.

CONCLUSIONS

Superhydrophobic surfaces were prepared by a chemical etching process: using the combination of hydrogen peroxide and a strong acid (i.e., hydrochloric acid or nitric acid) to obtain micro−nano hierarchical structures and subsequent treatment with FAS-17. Empirical grid maps were drawn with respect to different volumes of acid and H_2O_2, showing the wettability gradient: from hydrophobic to rose effect and finally to the lotus effect. It has been manifested that the surface modification could only be achieved at the oxidized region for the steel surface and that only in a specific concentration range of hydrogen peroxide could the high modification efficiency be obtained. The surfaces have demonstrated excellent anti-icing properties: for water dripping in overcooled conditions, the removal of water inhibited the freezing process; for the steam-freezing conditions, the low freezing point caused by the small, spherical droplets delayed the icing process. In addition, the prepared superhydrophobic surface possessed a superior resistance toward tape peeling 70 times with 3M adhesive tape under 31.2 kPa, 1.10 m of abrasion by 400 grid sandpaper at 16 kPa, and 3 h (~10 800 droplets) of water impacting. Furthermore, the as-prepared superhydrophobic surface exhibited outstanding anticorrosion properties in 3.5 wt % NaCl solution and good UV-durability against 50 h of UV-irradiation. This robust, durable, and anti-icing superhydrophobic surface may realize true industrial applications.

ASSOCIATED CONTENT

Supporting Information

Additional figures, a table, and pretreatment methods, as noted in the text, and Video S1, showing the tape-peeling test, and Video S2, showing the abrasion tests. This material is available free of charge via the Internet at http://pubs.acs.org.

DOI: 10.1021/acsami.5b00558
ACS Appl. Mater. Interfaces 2015, 7, 6260−6272

AUTHOR INFORMATION

Corresponding Author

*E-mail: xiongds@163.com.

Notes

The authors declare no competing financial interest.

ACKNOWLEDGMENTS

This work has received financial support from the National Natural Science Foundation of China (No. 11172142), Technological Innovation Funds of Jiangsu Province (No. BC2012011), Innovation of Graduate Student Training Plan in Jiangsu Province (No. KYZZ_0118), and project funding by the Priority Academic Program Development of Jiangsu Higher Education Institutions (PAPD).

REFERENCES

(1) Barthlott, W.; Neinhuis, C. Purity of the Sacred Lotus, or Escape from Contamination in Biological Surfaces. *Planta* **1997**, *202*, 1−8.

(2) Bhushan, B.; Jung, Y. C.; Niemietz, A.; Koch, K. Lotus-Like Biomimetic Hierarchical Structures Developed by the Self-Assembly of Tubular Plant Waxes. *Langmuir* **2009**, *25*, 1659−1666.

(3) Feng, L.; Li, S.; Li, Y.; Li, H.; Zhang, L.; Zhai, J.; Song, Y.; Liu, B.; Jiang, L.; Zhu, D. Super-Hydrophobic Surfaces: From Natural to Artificial. *Adv. Mater.* **2002**, *14*, 1857−1860.

(4) Barthlott, W.; Schimmel, T.; Wiersch, S.; Koch, K.; Brede, M.; Barczewski, M.; Walheim, S.; Weis, A.; Kaltenmaier, A.; Leder, A. The Salvinia Paradox: Superhydrophobic Surfaces with Hydrophilic Pins for Air Retention under Water. *Adv. Mater.* **2010**, *22*, 2325−2328.

(5) Yang, C.-Y.; Tsai, Y.-L.; Yang, C.-Y.; Sung, C.-K.; Yu, P.; Kuo, H.-C. Superhydrophobic, Antiadhesive, and Antireflective Surfaces Mediated by Hybrid Biomimetic Salvinia Leaf with Moth-Eye Structures. *Appl. Phys. Express* **2014**, *7*, 087001.

(6) Hu, D. L.; Chan, B.; Bush, J. W. The Hydrodynamics of Water Strider Locomotion. *Nature* **2003**, *424*, 663−666.

(7) Gao, X.; Jiang, L. Biophysics: Water-Repellent Legs of Water Striders. *Nature* **2004**, *432*, 36−36.

(8) Feng, L.; Zhang, Y.; Xi, J.; Zhu, Y.; Wang, N.; Xia, F.; Jiang, L. Petal Effect: A Superhydrophobic State with High Adhesive Force. *Langmuir* **2008**, *24*, 4114−4119.

(9) Xi, J.; Jiang, L. Biomimic Superhydrophobic Surface with High Adhesive Forces. *Ind. Eng. Chem. Res.* **2008**, *47*, 6354−6357.

(10) Bhushan, B. Gecko Feet: Natural Hairy Attachment Systems for Smart Adhesion. *Springer Handbook of Nanotechnology*; Springer: New York, 2010; pp 1553−1597.

(11) Bhushan, B. Gecko Feet: Natural Hairy Attachment Systems for Smart Adhesion. In *Nanotribology and Nanomechanics II*; Springer: New York, 2011; pp 701−767.

(12) Bhushan, B.; Jung, Y. C.; Koch, K. Micro-, Nano- and Hierarchical Structures for Superhydrophobicity, Self-Cleaning and Low Adhesion. *Philos. Trans. R. Soc. A* **2009**, *367*, 1631−1672.

(13) Fürstner, R.; Barthlott, W.; Neinhuis, C.; Walzel, P. Wetting and Self-Cleaning Properties of Artificial Superhydrophobic Surfaces. *Langmuir* **2005**, *21*, 956−961.

(14) Wang, N.; Xiong, D. Comparison of Micro-/Nano-Hierarchical and Nano-Scale Roughness of Silica Membranes in Terms of Wetting Behavior and Transparency. *Colloids Surf., A* **2014**, *446*, 8−14.

(15) Cao, L.; Jones, A. K.; Sikka, V. K.; Wu, J.; Gao, D. Anti-Icing Superhydrophobic Coatings. *Langmuir* **2009**, *25*, 12444−12448.

(16) Ruan, M.; Li, W.; Wang, B.; Deng, B.; Ma, F.; Yu, Z. Preparation and Anti-Icing Behavior of Superhydrophobic Surfaces on Aluminum Alloy Substrates. *Langmuir* **2013**, *29*, 8482−8491.

(17) Wang, N.; Xiong, D. Superhydrophobic Membranes on Metal Substrate and Their Corrosion Protection in Different Corrosive Media. *Appl. Surf. Sci.* **2014**, *305*, 603−608.

(18) Barkhudarov, P. M.; Shah, P. B.; Watkins, E. B.; Doshi, D. A.; Brinker, C. J.; Majewski, J. Corrosion Inhibition Using Superhydrophobic Films. *Corros. Sci.* **2008**, *50*, 897−902.

(19) Feng, L.; Zhang, Z.; Mai, Z.; Ma, Y.; Liu, B.; Jiang, L.; Zhu, D. A Super-Hydrophobic and Super-Oleophilic Coating Mesh Film for the Separation of Oil and Water. *Angew. Chem., Int. Ed.* **2004**, *43*, 2012−2014.

(20) Wang, C.-F.; Lin, S.-J. Robust Superhydrophobic/Superoleophilic Sponge for Effective Continuous Absorption and Expulsion of Oil Pollutants from Water. *ACS Appl. Mater. Interfaces* **2013**, *5*, 8861−8864.

(21) Li, J.; Shi, L.; Chen, Y.; Zhang, Y.; Guo, Z.; Su, B.-l.; Liu, W. Stable Superhydrophobic Coatings from Thiol-Ligand Nanocrystals and Their Application in Oil/Water Separation. *J. Mater. Chem.* **2012**, *22*, 9774−9781.

(22) Lim, J. I.; Kim, S.; Kim, S. H. Lotus-Leaf-Like Structured Heparin-Conjugated Poly(L-lactide-*co*-ε-caprolactone) as a Blood Compatible Material. *Colloids Surf., B* **2013**, *103*, 463−7.

(23) Loo, C.-Y.; Young, P. M.; Lee, W.-H.; Cavaliere, R.; Whitchurch, C. B.; Rohanizadeh, R. Superhydrophobic, Nanotextured Polyvinyl Chloride Films for Delaying *Pseudomonas aeruginosa* Attachment to Intubation Tubes and Medical Plastics. *Acta Biomater.* **2012**, *8*, 1881−1890.

(24) Udagawa, H. Drag Reduction of Newtonian Fluid in a Circular Pipe with a Highly Water-Repellent Wall. *J. Fluid Mech.* **1999**, *381*, 225−238.

(25) Daniello, R. J.; Waterhouse, N. E.; Rothstein, J. P. Drag Reduction in Turbulent Flows over Superhydrophobic Surfaces. *Phys. Fluids* **2009**, *21*, 085103.

(26) Jiang, L.; Zhao, Y.; Zhai, J. A Lotus-Leaf-Like Superhydrophobic Surface: A Porous Microsphere/Nanofiber Composite Film Prepared by Electrohydrodynamics. *Angew. Chem.* **2004**, *116*, 4438−4441.

(27) Jung, Y. C.; Bhushan, B. Contact Angle, Adhesion and Friction Properties of Micro-and Nanopatterned Polymers for Superhydrophobicity. *Nanotechnology* **2006**, *17*, 4970.

(28) Nakajima, A.; Hashimoto, K.; Watanabe, T.; Takai, K.; Yamauchi, G.; Fujishima, A. Transparent Superhydrophobic Thin Films with Self-Cleaning Properties. *Langmuir* **2000**, *16*, 7044−7047.

(29) Lee, Y.; Park, S. H.; Kim, K. B.; Lee, J. K. Fabrication of Hierarchical Structures on a Polymer Surface To Mimic Natural Superhydrophobic Surfaces. *Adv. Mater.* **2007**, *19*, 2330−2335.

(30) Ganesh, V. A.; Raut, H. K.; Nair, A. S.; Ramakrishna, S. A Review on Self-Cleaning Coatings. *J. Mater. Chem.* **2011**, *21*, 16304−16322.

(31) Song, J.; Xu, W.; Lu, Y. One-Step Electrochemical Machining of Superhydrophobic Surfaces on Aluminum Substrates. *J. Mater. Sci.* **2012**, *47*, 162−168.

(32) Yu, S.; Wang, X.; Wang, W.; Yao, Q.; Xu, J.; Xiong, W. A New Method for Preparing Bionic Multi Scale Superhydrophobic Functional Surface on X70 Pipeline Steel. *Appl. Surf. Sci.* **2013**, *271*, 149−155.

(33) Zheng, Z.; Azzaroni, O.; Zhou, F.; Huck, W. T. Topography Printing to Locally Control Wettability. *J. Am. Chem. Soc.* **2006**, *128*, 7730−7731.

(34) Xu, Q. F.; Mondal, B.; Lyons, A. M. Fabricating Superhydrophobic Polymer Surfaces with Excellent Abrasion Resistance by a Simple Lamination Templating Method. *ACS Appl. Mater. Interfaces* **2011**, *3*, 3508−3514.

(35) Nakayama, K.; Tsuji, E.; Aoki, Y.; Habazaki, H. Fabrication of Superoleophobic Hierarchical Surfaces for Low-Surface-Tension Liquids. *RSC Adv.* **2014**, *4*, 30927−30933.

(36) Yang, J.; Zhang, Z.; Men, X.; Xu, X.; Zhu, X.; Zhou, X.; Xue, Q. Rapid and Reversible Switching between Superoleophobicity and Superoleophilicity in Response to Counterion Exchange. *J. Colloid Interface Sci.* **2012**, *366*, 191−195.

(37) Xiu, Y.; Liu, Y.; Hess, D. W.; Wong, C. Mechanically Robust Superhydrophobicity on Hierarchically Structured Si Surfaces. *Nanotechnology* **2010**, *21*, 155705.

(38) Gupta, N.; Sasikala, S.; Barshilia, H. C. Corrosion Study of Superhydrophobic Magnesium Alloy AZ31 Surfaces Prepared by Wet Chemical Etching Process. *Nanosci. Nanotechnol. lett.* **2012**, *4*, 757−765.

(39) Peng, S.; Yang, X.; Tian, D.; Deng, W. Chemically Stable and Mechanically Durable Superamphiphobic Aluminum Surface with Micronano Binary Structure. *ACS Appl. Mater. Interfaces* **2014**, *6*, 15188−15197.

DOI: 10.1021/acsami.5b00558
ACS Appl. Mater. Interfaces 2015, 7, 6260−6272

(40) Qian, B.; Shen, Z. Fabrication of Superhydrophobic Surfaces by Dislocation-Selective Chemical Etching on Aluminum, Copper, and Zinc Substrates. *Langmuir* **2005**, *21*, 9007−9009.
(41) Qu, M.; Zhang, B.; Song, S.; Chen, L.; Zhang, J.; Cao, X. Fabrication of Superhydrophobic Surfaces on Engineering Materials by a Solution-Immersion Process. *Adv. Funct. Mater.* **2007**, *17*, 593−596.
(42) Pujari, S. P.; Scheres, L.; Marcelis, A.; Zuilhof, H. Covalent Surface Modification of Oxide Surfaces. *Angew. Chem., Int. Ed.* **2014**, *53*, 6322−6356.
(43) Groten, J.; Rühe, J. R. Surfaces with Combined Microscale and Nanoscale Structures: A Route to Mechanically Stable Superhydrophobic Surfaces? *Langmuir* **2013**, *29*, 3765−3772.
(44) Wang, B.; Li, J.; Wang, G.; Liang, W.; Zhang, Y.; Shi, L.; Guo, Z.; Liu, W. Methodology for Robust Superhydrophobic Fabrics and Sponges from in Situ Growth of Transition Metal/Metal Oxide Nanocrystals with Thiol Modification and Their Applications in Oil/Water Separation. *ACS Appl. Mater. Interfaces* **2013**, *5*, 1827−1839.
(45) Zhou, X.; Zhang, Z.; Xu, X.; Guo, F.; Zhu, X.; Men, X.; Ge, B. Robust and Durable Superhydrophobic Cotton Fabrics for Oil/Water Separation. *ACS Appl. Mater. Interfaces* **2013**, *5*, 7208−7214.
(46) Zhang, J.; Li, B.; Wu, L.; Wang, A. Facile Preparation of Durable and Robust Superhydrophobic Textiles by Dip Coating in Nanocomposite Solution of Organosilanes. *Chem. Commun.* **2013**, *49*, 11509−11511.
(47) Ge, B.; Zhang, Z.; Zhu, X.; Ren, G.; Men, X.; Zhou, X. A Magnetically Superhydrophobic Bulk Material for Oil Removal. *Colloids Surf., A* **2013**, *429*, 129−133.
(48) Muthiah, P.; Bhushan, B.; Yun, K.; Kondo, H. Dual-Layered-Coated Mechanically-Durable Superomniphobic Surfaces with Anti-Smudge Properties. *J. Colloid Interface Sci.* **2013**, *409*, 227−236.
(49) Yin, L.; Yang, J.; Tang, Y.; Chen, L.; Liu, C.; Tang, H.; Li, C. Mechanical Durability of Superhydrophobic and Oleophobic Copper Meshes. *Appl. Surf. Sci.* **2014**, *316*, 259−263.
(50) Deng, D.; Prendergast, D. P.; MacFarlane, J.; Bagatin, R.; Stellacci, F.; Gschwend, P. M. Hydrophobic Meshes for Oil Spill Recovery Devices. *ACS Appl. Mater. Interfaces* **2013**, *5*, 774−781.
(51) Chen, J.; Dou, R.; Cui, D.; Zhang, Q.; Zhang, Y.; Xu, F.; Zhou, X.; Wang, J.; Song, Y.; Jiang, L. Robust Prototypical Anti-Icing Coatings with a Self-Lubricating Liquid Water Layer between Ice and Substrate. *ACS Appl. Mater. Interfaces* **2013**, *5*, 4026−4030.
(52) Boinovich, L. B.; Emelyanenko, A. M.; Ivanov, V. K.; Pashinin, A. S. Durable Icephobic Coating for Stainless Steel. *ACS Appl. Mater. Interfaces* **2013**, *5*, 2549−2554.
(53) Kulinich, S.; Farhadi, S.; Nose, K.; Du, X. Superhydrophobic Surfaces: Are They Really Ice-Repellent? *Langmuir* **2010**, *27*, 25−29.
(54) Yildirim, A.; Khudiyev, T.; Daglar, B.; Budunoglu, H.; Okyay, A. K.; Bayindir, M. Superhydrophobic and Omnidirectional Antireflective Surfaces from Nanostructured Ormosil Colloids. *ACS Appl. Mater. Interfaces* **2013**, *5*, 853−860.
(55) Liu, L.; Xu, F.; Ma, L. Facile Fabrication of a Superhydrophobic Cu Surface via a Selective Etching of High-Energy Facets. *J. Phys. Chem. C* **2012**, *116*, 18722−18727.
(56) Hozumi, A.; Kim, B.; McCarthy, T. J. Hydrophobicity of Perfluoroalkyl Isocyanate Monolayers on Oxidized Aluminum Surfaces. *Langmuir* **2009**, *25*, 6834−6840.
(57) Saleema, N.; Sarkar, D.; Paynter, R.; Chen, X.-G. Superhydrophobic Aluminum Alloy Surfaces by a Novel One-Step Process. *ACS Appl. Mater. Interfaces* **2010**, *2*, 2500−2502.
(58) Guo, Z.; Zhou, F.; Hao, J.; Liu, W. Stable Biomimetic Super-Hydrophobic Engineering Materials. *J. Am. Chem. Soc.* **2005**, *127*, 15670−15671.
(59) Lum, K.; Chandler, D.; Weeks, J. D. Hydrophobicity at Small and Large Length Scales. *J. Phys. Chem. B* **1999**, *103*, 4570−4577.
(60) Boscher, N. D.; Vaché, V.; Carminati, P.; Grysan, P.; Choquet, P. A Simple and Scalable Approach Towards the Preparation of Superhydrophobic Surfaces—Importance of the Surface Roughness Skewness. *J. Mater. Chem. A* **2014**, *2*, 5744−5750.
(61) Zhan, X.; Yan, Y.; Zhang, Q.; Chen, F. A Novel Superhydrophobic Hybrid Nanocomposite Material Prepared by Surface-Initiated Agent ATRP and Its Anti-Icing Properties. *J. Mater. Chem. A* **2014**, *2*, 9390−9399.
(62) Deng, X.; Mammen, L.; Zhao, Y.; Lellig, P.; Müllen, K.; Li, C.; Butt, H. J.; Vollmer, D. Transparent, Thermally Stable and Mechanically Robust Superhydrophobic Surfaces Made from Porous Silica Capsules. *Adv. Mater.* **2011**, *23*, 2962−2965.
(63) Lee, S.-M.; Kim, K.-S.; Pippel, E.; Kim, S.; Kim, J.-H.; Lee, H.-J. Facile Route toward Mechanically Stable Superhydrophobic Copper Using Oxidation−Reduction Induced Morphology Changes. *J. Phys. Chem. C* **2012**, *116*, 2781−2790.
(64) She, Z.; Li, Q.; Wang, Z.; Li, L.; Chen, F.; Zhou, J. Novel Method for Controllable Fabrication of a Superhydrophobic CuO Surface on AZ91D Magnesium Alloy. *ACS Appl. Mater. Interfaces* **2012**, *4*, 4348−4356.
(65) Barthwal, S.; Kim, Y. S.; Lim, S.-H. Mechanically Robust Superamphiphobic Aluminum Surface with Nanopore-Embedded Microtexture. *Langmuir* **2013**, *29*, 11966−11974.
(66) Su, F.; Kai, Y. Facile Fabrication of Superhydrophobic Surface with Excellent Mechanical Abrasion and Corrosion Resistance on Copper Substrate by a Novel Method. *ACS Appl. Mater. Interfaces* **2014**, *6*, 8762−8770.
(67) Zhang, Y.; Ge, D.; Yang, S. Spray-Coating of Superhydrophobic Aluminum Alloys with Enhanced Mechanical Robustness. *J. Colloid Interface Sci.* **2014**, *423*, 101−107.
(68) Cho, H.; Kim, D.; Lee, C.; Hwang, W. A Simple Fabrication Method for Mechanically Robust Superhydrophobic Surface by Hierarchical Aluminum Hydroxide Structures. *Curr. Appl. Phys.* **2013**, *13*, 762−767.
(69) She, Z.; Li, Q.; Wang, Z.; Li, L.; Chen, F.; Zhou, J. Researching the Fabrication of Anticorrosion Superhydrophobic Surface on Magnesium Alloy and Its Mechanical Stability and Durability. *Chem. Eng. J.* **2013**, *228*, 415−424.
(70) Ou, J.; Hu, W.; Liu, S.; Xue, M.; Wang, F.; Li, W. Superoleophobic Textured Copper Surfaces Fabricated by Chemical Etching/Oxidation and Surface Fluorination. *ACS Appl. Mater. Interfaces* **2013**, *5*, 10035−10041.
(71) Zhou, S.; Ding, X.; Wu, L. Fabrication of Ambient-Curable Superhydrophobic Fluoropolysiloxane TiO_2 Nanocomposite Coatings with Good Mechanical Properties and Durability. *Prog. Org. Coat.* **2013**, *76*, 563−570.
(72) Xue, C.-H.; Yin, W.; Zhang, P.; Zhang, J.; Ji, P.-T.; Jia, S.-T. UV-Durable Superhydrophobic Textiles with UV-Shielding Properties by Introduction of Zno/SiO_2 Core/Shell Nanorods on Pet Fibers and Hydrophobization. *Colloids Surf., A* **2013**, *427*, 7−12.
(73) Zhang, S.; Li, Q.; Chen, B.; Yang, X. Preparation and Corrosion Resistance Studies of Nanometric Sol−Gel-Based CeO_2 Film with a Chromium-Free Pretreatment on AZ91D Magnesium Alloy. *Electrochim. Acta* **2010**, *55*, 870−877.
(74) Ou, J.; Hu, W.; Xue, M.; Wang, F.; Li, W. Superhydrophobic Surfaces on Light Alloy Substrates Fabricated by a Versatile Process and Their Corrosion Protection. *ACS Appl. Mater. Interfaces* **2013**, *5*, 3101−3107.
(75) Darmanin, T.; Guittard, F. Recent Advances in the Potential Applications of Bioinspired Superhydrophobic Materials. *J. Mater. Chem. A* **2014**, *2*, 16319−16359.

DOI: 10.1021/acsami.5b00558
ACS Appl. Mater. Interfaces 2015, 7, 6260−6272